An axisymmetric incompressible lattice BGK model for simulation of the pulsatile flow in a circular pipe

T. S. Lee[‡], Haibo Huang[*,†] and Chang Shu[§]

Mechanical Engineering, National University of Singapore, Singapore, Singapore

SUMMARY

Applying the idea of Halliday *et al.*, through inserting the 'source' term into the two-dimensional lattice Boltzmann equation to recover the incompressible Navier–Stokes equation in the cylindrical coordinates, an axisymmetric incompressible Lattice-BGK D2Q9 model was proposed here to simulate the pulsatile flows in a circular pipe. The pulsatile flows in a circular pipe with $1 < Re < 2000$ (Reynolds number is based on pipe's diameter), Womersley number $1 < \alpha < 25$ were investigated and compared with the exact analytical solutions. The excellent agreements between numerical and the analytical solution validate our model. The effect of schemes to implement pressure gradient and the model's spatial accuracy were also discussed. To show the performance of the proposed model, the same problems were also simulated by Halliday's axisymmetric model which derived from standard LBM and the three-dimensional incompressible LBGK model. It is observed that the present model reduces the compressibility effect in Halliday's model and is much more efficient than the LBGK D3Q19 model for an axisymmetric pulsatile flow problem. Copyright © 2005 John Wiley & Sons, Ltd.

KEY WORDS: lattice Boltzmann method; axisymmetric; incompressible Navier–Stokes equation

1. INTRODUCTION

The lattice Boltzmann method (LBM) has been proposed as an alternative numerical scheme for solving the incompressible Navier–Stokes (NS) equations [1, 2]. Among different lattice Boltzmann equation (LBE) models in application, the lattice Bhatnagar–Gross–Krook (LBGK) model is the simplest one because it only involves one scalar relaxation parameter and a simple equilibrium momentum distribution function [3]. If the density fluctuation can be neglected, the incompressible Navier–Stokes equation can be recovered from a LBE through the Chapman–Enskog procedure [4]. However, in LBM, the density may fluctuate to a great extent in flows with large pressure gradient because the pressure and density variations satisfy the equation of

*Correspondence to: Haibo Huang, Mechanical Engineering, National University of Singapore, Singapore, Singapore.
[†]E-mail: g0301108@nus.edu.sg
[‡]E-mail: mpeleets@nus.edu.sg
[§]E-mail: mpeshuc@nus.edu.sg

Copyright © 2005 John Wiley & Sons, Ltd.

states of an isothermal gas given by $\Delta p = c_s^2 \Delta \rho$ [4], where c_s^2 is a constant. In many previous studies [4–6], the compressibility effect of standard LBGK model has been highlighted.

Some incompressible models were proposed to eliminate the compressibility effect of the standard LBGK model [6, 7]. One of the most successful incompressible LBGK model was proposed by He and Luo in 1997 [6]. The incompressible LBGK model was validated by steady plane poiseuille flow and the unsteady 2D Womersley flow. In their model, the compressibility effect of the order $o(M^2)$ is explicitly eliminated [6].

In the past, besides the above study [6] on 2D Womersley flow, Cosgrove et al. [8] also simulated the 2D Womersley flow with $400 < Re_\delta < 1000$ and $1 < \alpha < 31$. Artoli et al. [9] studied the accuracy of 2D Womersley flow using 2D 9-velocity (D2Q9) model with different boundary conditions.

Since we are interested in studying blood flow in large arteries, we would like to simulate the 3D oscillatory flow in pipes. However, when it comes to the problems of 3D axisymmetric Womersley flow [5] or 3D steady flows [10] in tube, most of previous studies [5, 10] still recourse to the 3D LBGK model and using the 3D cubic lattices with proper curvature wall boundary treatment directly. That means a large mesh size and it is not so efficient to simulate such an axisymmetric problem in that way.

To simulate the axisymmetric flow more efficiently, in 2001, Halliday et al. [3] proposed an axisymmetric D2Q9 model for the steady 3D axisymmetric flow problems and it seems very successful for steady tube flow. Later Niu et al. [11] further derived an axisymmetric model for simulation of the Taylor–Couette flows. The main idea of the model is inserting several spatial and velocity-dependent 'source' terms into the adjusted evaluation equation for the lattice fluid's momentum distribution [3], which is similar to the conventional CFD methods.

However, the axisymmetric D2Q9 model proposed by Halliday et al. [3] and Niu et al. [11] is derived from the standard D2Q9 model. When we simulate the 2D Womersley flow with the standard D2Q9 model, the solution involves significant compressibility effect [6]. Similar circumstances may appear when using the axisymmetric model proposed by Halliday et al. [3].

Till today, simulation of the pulsatile flow in circular pipe using incompressible axisymmetric D2Q9 model has not been reported. In this paper an axisymmetric incompressible D2Q9 model is proposed. To validate and evaluate the performance of the model, 3D Womersley flow simulations were performed. The 3D Womersley flow (pulsatile flow in axisymmetric pipe) is driven by periodic pressure gradient at the inlet of the pipe. Since a typical Reynolds number in the abdominal aorta is 1250 and a typical Womersley number $\alpha = 8$ [5], the parameters of most cases in this paper are close to these two values.

For 3D Womersley flow simulations, two different schemes were adopted to implement the oscillatory pressure gradient. One is applying an equivalent body force in the post-collision step, the other is specifying the oscillatory or fixed pressure at ends of the pipe directly. Most of the previous studies [3, 8] adopt the first scheme. That may introduce the influence of the body force and since there are different flow conditions at the outlet of arteries this scheme may be unreal for the vascular flow simulation [5].

The effects of different schemes to implement the oscillatory pressure gradient and the model's spatial accuracy were also discussed here. To show the performance of the proposed model, the same problem was also simulated by the incompressible LBGK 3D 19-velocity (D3Q19) model. Detailed comparison of CPU time and accuracy of numerical results between our model and 3D model is given. The comparison demonstrates that the present axisymmetric

model is much more efficient than the LBGK D3Q19 model for an axisymmetric pulsatile flow problem in terms of CPU time and memory.

2. NUMERICAL METHODS

For the incompressible internal flow in a circular pipe if we assume that the flow is axisymmetric, the azimuthal velocity u_ϕ and ϕ coordinate derivatives vanish from the incompressible continuity and Navier–Stokes equations.

Hence the continuity equation is

$$\frac{\partial u_x}{\partial x} + \frac{\partial u_r}{\partial r} = -\frac{u_r}{r} \tag{1}$$

The axial and radial velocities u_x, u_r satisfying two momentum equations in the two spatial coordinates x and r are

$$\frac{\mathrm{D}u_x}{\mathrm{D}t} = -\frac{1}{\rho_0}\frac{\partial p}{\partial x} + v\nabla^2 u_x + \frac{v}{r}\frac{\partial u_x}{\partial r} \tag{2}$$

$$\frac{\mathrm{D}u_r}{\mathrm{D}t} = -\frac{1}{\rho_0}\frac{\partial p}{\partial r} + v\nabla^2 u_r + \frac{v}{r}\left(\frac{\partial u_r}{\partial r} - \frac{u_r}{r}\right) \tag{3}$$

2.1. Axisymmetric incompressible LBGK model

Here, in our study, the incompressible LBGK D2Q9 model [6] was employed to further derive our axisymmetric incompressible model. Theoretically the LBE simulated the compressible Navier–Stokes equation instead of the incompressible one, because the spatial density variation is not zero in LBE simulations. In order to correctly simulate incompressible Navier–Stokes equation in practice, one must ensure that the Mach number is low and the density fluctuation ($\delta\rho$) is of order $o(M^2)$ [6]. The derivation procedure and additional limit $L_x/(c_sT) \ll 1$ is illustrated in Appendix A. From the derivation, Equations (1)–(3) can be recovered.

For our present axisymmetric incompressible D2Q9 model, the nine discrete velocities are as follows:

$$\mathbf{e}_i = \begin{cases} (0,0), & i=0 \\ (\cos[(i-1)\pi/2], \sin[(i-1)\pi/2])c, & i=1,2,3,4 \\ \sqrt{2}(\cos[(i-5)\pi/2 + \pi/4], \sin[(i-5)\pi/2 + \pi/4])c, & i=5,6,7,8 \end{cases} \tag{4}$$

where $c = \delta_x/\delta_t$, δ_x and δ_t are the lattice spacing and time step size. In this paper $c=1$. The discrete velocities were also illustrated in Figure 1.

In our axisymmetric D2Q9 model, $f_i(x,r,t)$ is the distribution function for particles with velocity $\mathbf{e}_i$ at position (x,r) and time t. The macroscopic pressure p and momentum $\rho_0\mathbf{u}$ are defined as

$$\sum_{i=0}^{8} f_i = p/c_s^2, \quad \sum_{i=0}^{8} f_i e_{i\alpha} = \rho_0 u_\alpha \tag{5}$$

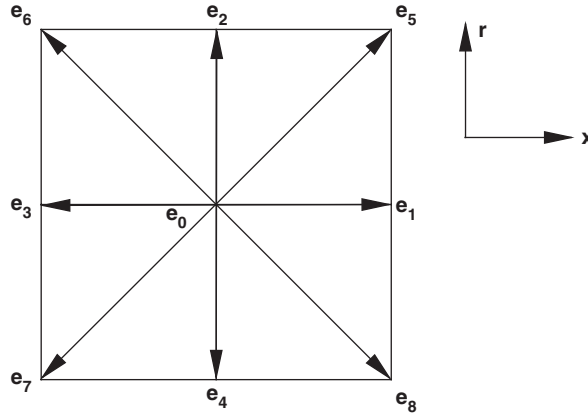where ρ_0 is the density of fluid.

Figure 1. The discrete velocity for axisymmetric D2Q9 model.

The two main steps of LBGK D2Q9 model are collision and streaming. In the collision step, a group of calculations from (6a) to (6d) are implemented:

$$f_i^{\text{ne}} = f_i(x,r,t) - f_i^{\text{eq}}(x,r,t) \tag{6a}$$

$$h_i^{(1)} = -\frac{\omega_i \rho_0 u_r}{r} \tag{6b}$$

$$h_i^{(2)} = \omega_i \frac{3\nu}{r}[\partial_y p + \rho_0 \partial_x u_x u_r + \rho_0 \partial_r u_r u_r + \rho_0(\partial_r u_x - \partial_x u_r)e_{ix}] \tag{6c}$$

$$f_i^{+}(x,r,t) = f_i^{\text{eq}}(x,r,t) + \left(1 - \frac{1}{\tau}\right)f_i^{\text{ne}} + \delta_t h_i^{(1)} + \delta_t^2 h_i^{(2)} \tag{6d}$$

where f_i^{eq} is the equilibrium momentum distribution function and f_i^{ne} is the non-equilibrium part of distribution function. $h_i^{(1)}$ and $h_i^{(2)}$ are the 'source' terms added into the collision step. The derivation procedure of $h_i^{(1)}$ and $h_i^{(2)}$ was illustrated in Appendix A. In above expressions, $\omega_0 = 4/9$, $\omega_i = 1/9$, $(i = 1,2,3,4)$, $\omega_i = 1/36$, $(i = 5,6,7,8)$. f_i^{eq} can be obtained through the following equation [6]:

$$f_i^{\text{eq}}(x,r,t) = \omega_i \frac{p}{c_s^2} + \omega_i \rho_0 \left[\frac{\mathbf{e}_i \cdot \mathbf{u}}{c_s^2} + \frac{(\mathbf{e}_i \cdot \mathbf{u})^2}{2c_s^4} - \frac{\mathbf{u}^2}{2c_s^2}\right], \quad i = 0,1,2,\ldots,8 \tag{7}$$

It is noticed that the main difference between the above incompressible D2Q9 model and the standard D2Q9 model is the form of Equation (7). In the above formulas (6c) and (6d), the relaxation time constant τ and the fluid viscosity satisfy equation $\nu = (2\tau - 1)\delta_x/6$. In the streaming step, the new distribution function value obtained from (6d) would propagate to the neighbouring eight lattices. That can be implemented by the following Equation (8), which would be applied on all uniform lattices:

$$f_i(x + e_{ix}\delta_t, r + e_{ir}\delta_t, t + \delta_t) = f_i^{+}(x,r,t) \tag{8}$$

Here, in this paper $\delta_t = \delta_x = 1$.

For the velocity derivations in above Equation (6c), the terms $\partial_r u_x + \partial_x u_r$, $\partial_x u_x$ and $\partial_r u_r$ can be obtained through Equation (9) with $\alpha = x, \beta = r$; $\alpha = \beta = x$; $\alpha = \beta = r$, respectively:

$$\rho_0 \nu (\partial_\beta u_\alpha + \partial_\alpha u_\beta) = -\left(1 - \frac{1}{2\tau}\right) \sum_{i=0}^{8} f_i^{(1)} e_{i\alpha} e_{i\beta} = -\left(1 - \frac{1}{2\tau}\right) \sum_{i=0}^{8} f_i^{ne} e_{i\alpha} e_{i\beta} + o(\varepsilon^2) \qquad (9)$$

For the term $\partial_r u_x - \partial_x u_r$ in Equation (6c), it is equal to $(\partial_r u_x + \partial_x u_r) - 2\partial_x u_r$. Since $(\partial_r u_x + \partial_x u_r)$ can be easily obtained by Equation (9), only the value of $\partial_x u_r$ is left unknown to determine $\partial_r u_x - \partial_x u_r$. Here we recourse to finite difference method to obtain $\partial_x u_r$ at lattice node (i, j), which can be calculated by Equation (10):

$$(\partial_x u_r)_{i,j} = ((u_r)_{i+1,j} - (u_r)_{i-1,j})/(2\delta x) \qquad (10)$$

The values of $\partial_r u_x + \partial_x u_r$, $\partial_x u_x$, $\partial_r u_r$, and $\partial_x u_r$ for the lattice nodes which are just on the wall boundary can also be calculated from Equations (9) and (10). Obtaining these values for lattice nodes on the periodic boundary is also easy. However, to obtain these values for the nodes on the inlet/outlet pressure-specified boundary, these values are extrapolated from those of the inner nodes.

2.2. Boundary condition

To implement the oscillatory pressure gradient, two schemes can be applied. One is applying an equivalent oscillatory body force [8] the other is simply specifying oscillatory pressure at the inlet boundary and fixing the outlet pressure [6].

To apply an equivalent body force, the periodic boundary conditions are imposed at the open ends of the pipe and in the collision step, after step (6d) was implemented, a further post-collision step is necessary:

$$f_i^+(x,r,t) = f_i^+(x,r,t) + \omega_i F_\alpha e_{i\alpha}/c_s^2, \quad i = 1, 2, \ldots, 8 \qquad (11)$$

where $\mathbf{F} = (p^* \cos(\omega t), 0)$ is the body force and p^* is the maximum amplitude of the oscillatory pressure gradient. In this paper, if it is not mentioned explicitly, the oscillatory pressure gradient was implemented in this way.

On the other hand, in our study, the inlet/outlet pressure boundary condition was also applied because the pressure gradient cannot always be replaced by an external force in LBGK computations. Some pressure boundary condition treatments have been proposed in previous LBM studies [12, 13]. Here the method proposed by Guo *et al.* [12] was adopted for its simplicity. If specifying oscillatory pressure at inlet boundary condition and fixing the outlet pressure, the corresponding velocity value in these boundaries was extrapolated from the next inner nodes. Hence, the equilibrium part of distribution function can be determined from the above Equation (7) and the non-equilibrium part of distribution function can be obtained through extrapolation [12]. So, the collision step for boundary nodes can be implemented normally as inner nodes.

For wall boundary conditions, it is well known that the most commonly applied in LBM is bounce back model [5]. However, for the 3D circular pipe flow problem, to treat the curvature wall boundary in uniform cubic lattices, original bounce back model is not accurate enough for curvature boundary [5]. For direct 3D simulation, in this study, the non-equilibrium distribution function extrapolation method [14] was applied for curvature wall boundary. In

the method, the velocity on 'wall nodes' (lattice nodes outside and most near to physical boundary) is obtained from extrapolation and p-value obtained from the nearest 'fluid node' (lattice nodes inside physical boundary), hence the equilibrium distribution function for 'wall nodes' can be obtained through Equation (7). With corresponding non-equilibrium distribution function extrapolated from the 'fluid nodes', the collision step on 'wall nodes' can be fulfilled. This treatment is proved to be second order in space [14].

When our 2D axisymmetric incompressible model was applied to study the axisymmetric pipe flows, the non-equilibrium distribution function extrapolation method [14] for wall boundary was also adopted. To apply this wall boundary treatment, an additional layer outside the wall boundary is included.

3. RESULTS AND DISCUSSION

The 3D Womersley flow (pulsatile flow in axisymmetric pipe) is driven by periodic pressure gradient at the inlet of the pipe. In the followings, p^* is the maximum amplitude of the sinusoidally varying pressure gradient.

$$\frac{\partial p}{\partial x} = -p^* e^{i\omega t} \tag{12}$$

R is defined as the radius of the circular pipe. ω is the angular frequency and v is the kinetic viscosity of fluid. The Reynolds number is defined as $Re = 2U_c R/v$, U_c is the characteristic velocity defined as

$$U_c = \frac{p^* \alpha^2}{4\omega\rho} = \frac{p^* R^2}{4\rho v} \tag{13}$$

which is the velocity that would be observed at the centre of the tube if a constant forcing term p^* was applied in the limit of $\alpha \to 0$. The Womersley number is defined as $\alpha = R\sqrt{\omega/v}$. The Strouhal number is defined as $St = R/(U_c T)$, where T is the sampling period.

The analytical solution for axisymmetric pipe pulsatile flow [5] is

$$u(r,t) = Re\left\{ \frac{p^*}{i\omega\rho_0} \left[1 - \frac{J_0[\frac{1}{\sqrt{2}}(-\alpha + i\alpha)(r/R)]}{J_0[\frac{1}{\sqrt{2}}(-\alpha + i\alpha)]} \right] e^{i\omega t} \right\} \tag{14}$$

where J_0 is the zeroth-order Bessel function of the first type.

All the simulations in this paper began with an initial condition of zero velocity every where, and an initial run of $10T$ steps.

It should be noticed that the maximum velocity U_{max} appeared in tube axis during a sampling period would be less than the character velocity U_c for case $\alpha > 0$. For case $\alpha \gg 1$, the maximum velocity U_{max} would be much less than U_c. This is illustrated in Figure 2, which shows the normalized maximum velocity in tube axis U_{max}/U_c, and the phase lag of the velocity field, ζ (normalized by π), as function of α. In the figure, the numerical results agree well with the analytical solution. It seems that when oscillatory pressure gradient changes very fast it is impossible for velocity field to reach the fully developed velocity profile with maximum value U_c.
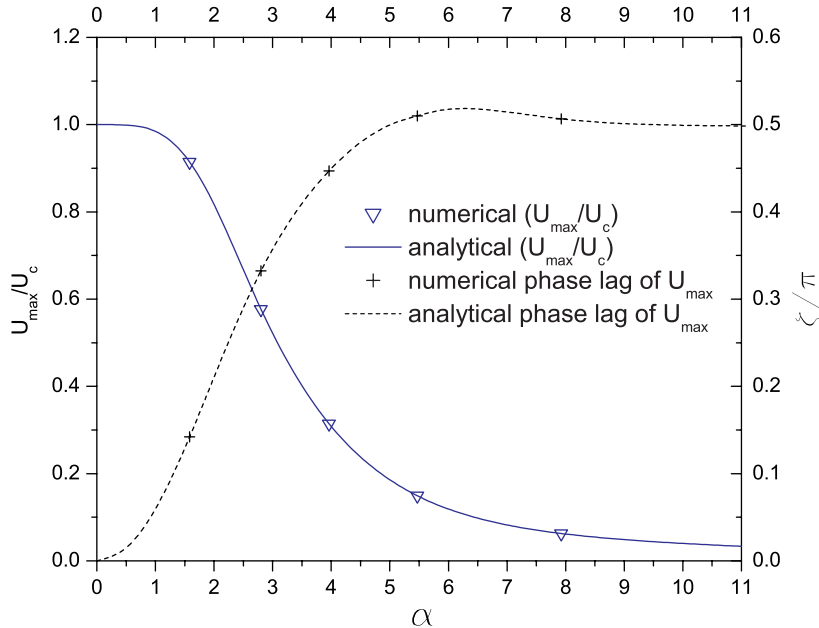
Figure 2. Maximum velocity in the axis of tube and the phase lag as function of Womersley number.

3.1. Converge criterion and spatial accuracy

To evaluate the error between the numerical and analytical solution, we introduce a velocity error formula which is illustrated in (15). At each time step the error can be defined as

$$\xi = \frac{\sum_i |u(r_i) - u_a(r_i)|}{\sum_i |u_a(r_i)|} \tag{15}$$

where $u(r_i)$ is the numerical solution, $u_a(r_i)$ is the analytical velocity at r_i in middle pipe. The overall average error $\langle \xi \rangle$ is averaged over the period T. For all the cases in this paper, the convergence criterion was set as follows:

$$\frac{\sum_x |u(\mathbf{x}, t + T) - u(\mathbf{x}, t)|}{\sum_x |u(\mathbf{x}, t + T)|} \leqslant 10^{-6} \tag{16}$$

where t was usually chosen as $t = 1 + nT$ in this paper.

Here in all cases, the pipe length was chosen as $2N_r$ [8], where N_r is the number of lattice nodes in the diameter (usually N_r excludes the upper and lower extra layers outside the wall boundary). The global errors behaviour for $\alpha = 7.927$ and 3.171 is illustrated in Figure 3. For a certain α, as N_r was increased α was kept constant by varying the period T accordingly within the range $T > 10^3$. For the above α, the corresponding τ was kept 0.6 and 1.0. In Figure 3, the solid lines represent the linear fits, and the slope of the lines are -1.89 ($\alpha = 7.927$) and -2.02 ($\alpha = 3.171$). The figure demonstrates that current LBGK model incorporating the extrapolation wall boundary condition and the forcing term is second order in space.
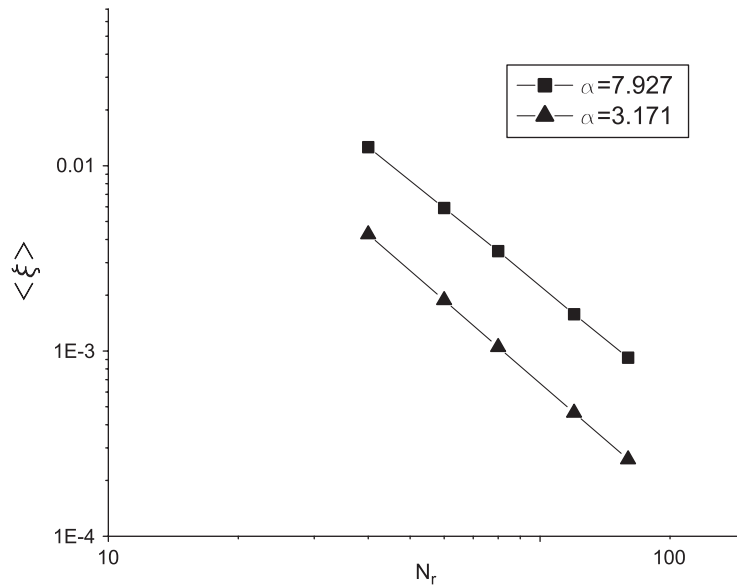
Figure 3. The global error $\langle\xi\rangle$ as a function of the pipe diameter N_r for $\alpha = 7.927$ and $\alpha = 3.171$.

3.2. Effect of Womersley number on flow pattern

As a typical Reynolds number in the abdominal aorta is about 1250 and a typical Womersley number $\alpha = 8$ [5], in our simulation, firstly the case of $Re = 1200$, $\alpha = 7.927$, $T = 1200$, $\tau = 0.6$ was performed, $N_r = 41$ and the corresponding $U_c = 1.0$. The exact analytical solutions of Equation (14) were compared to numerically evaluated velocity profiles along the diameter in Figures 4(a) and (b). The velocity is normalized by U_c. The r-axis is non-dimensionalized by dividing by the radius of the tube as indicated in Figure 4. Although in this case $U_c = 1.0$, the U_{max} observed in whole oscillatory period is only about 0.063, $M = 0.063\sqrt{3} \approx 0.109 \ll 1$, which is consistent with the limit of LBM.

In this case, parameters $T = 1200$, $\tau = 0.6$, $U_c = 1.0$ were chosen to avoid numerical stability and save computational time because if $U_c = 0.1$, to fix the parameter Re and α and the same mesh system, the v should be $1/300$, and then τ is 0.51, which is very close to 0.5, numerical instability may appear. On the other hand, the corresponding T value should be 12 000 while not just 1200. Hence much more CPU time is required. Anyway, $U_c = 1.0$ in this case is correct because $M \ll 1$.

Here, in the above case, the overall numerical average error is about 1.23%. While Artoli et al. [5] mentioned that the overall average error for almost the same 3D case is around 7% using the curve boundary condition proposed by Bouzidi et al. [15]. The present better performance may be due to our axisymmetric incompressible D2Q9 model eliminating the compressibility effect while the D3Q19 model applied by Artoli et al. [5] involves the effect and our second-order extrapolation wall boundary treatments may also account for the better performance.

Figures 5(a) and (b) show the velocity evolution of an oscillation over half a period for $\alpha = 1.373$ and 24.56, respectively. For the case illustrated in Figure 5(a), $Re = 1.2$, $\tau = 1.5$,
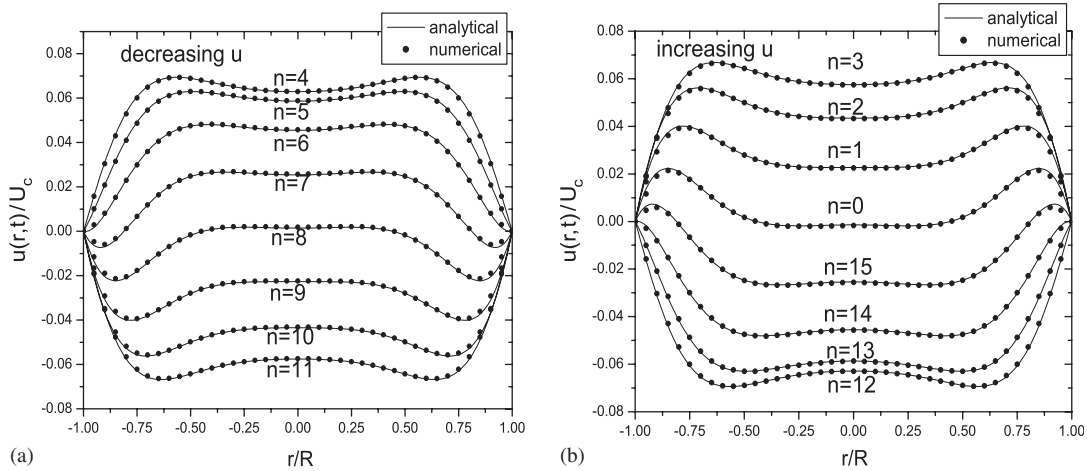
Figure 4. Profiles of: (a) decreasing; and (b) increasing velocities along the diameter of a tube for $\alpha = 7.927$, $T = 1200$, $Re = 1200$, $\tau = 0.6$, at $t = nT/16$ ($n = 0, \ldots, 15$) ($U_c = 1.0$, actually $U_{max} \sim 0.07$).
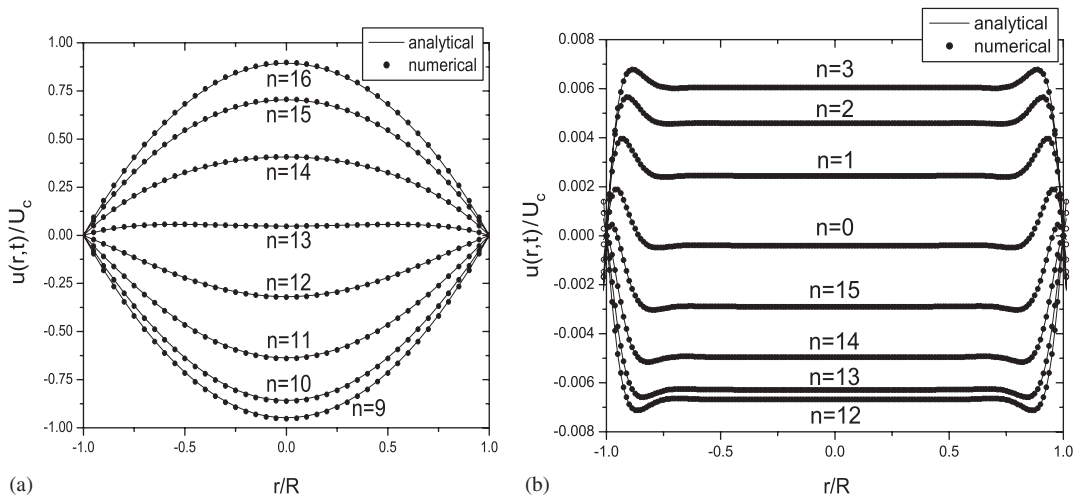

Figure 5. Velocity profile along the diameter over half a period: (a) $\alpha = 1.373$; and (b) $\alpha = 24.560$.

$T = 4000$, $U_c = 0.01$, $N_r = 41$, which is a viscous-dominated system [8]. For case illustrated in Figure 5(b), $Re = 1920$, $\tau = 0.7$, $T = 1000$, $U_c = 0.8$, $N_r = 161$, which is a momentum-dominated system in the laminar regime [8].

Since shear stress plays a crucial role in the progression of atherosclerosis. The shear stress tensor computation is important. In our 3D axisymmetric problem, the shear stress tensor σ_{xr} can be obtained conveniently from Equation (9). The calculation is usually implemented during the collision process. It is convenient to get shear stress tensor in LBM. Here we give an
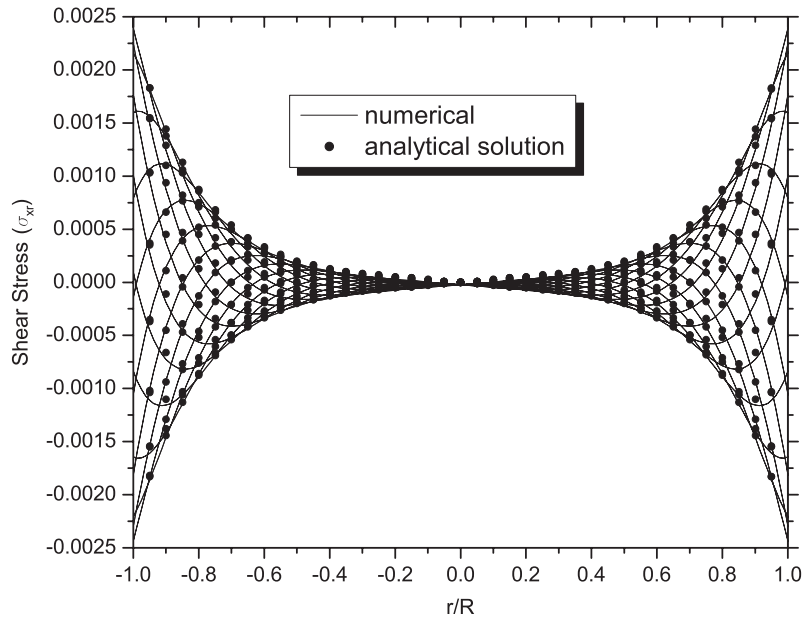
Figure 6. Shear stress, $Re = 1200$, $\tau = 0.6$, $\alpha = 7.927$, $T = 1200$ in a oscillatory tube flow, the measurements are taken at $t = nT/16$, $n = 0, 1, \ldots, 16$.

Table I. The overall average error $\langle \xi \rangle$ comparison for two schemes to implement the pressure gradient.

Cases	Scheme	
	Scheme of addition force term $\langle \xi \rangle$	Scheme of specify pressure on inlet/outlet BC $\langle \xi \rangle$
$Re = 12$, $p^* = 10^{-5}$	7.65e-3	7.30e-3
$Re = 120$, $p^* = 0.0001$	7.02e-3	1.81e-2
$Re = 600$, $p^* = 0.0005$	6.92e-3	6.97e-2

example with $\alpha = 7.927$, $T = 1200$, $\tau = 0.6$, $Re = 1200$, $N_r = 41$. In Figure 6, the analytical solutions were compared to numerically evaluated shear stress along the diameter at time $t = nT/16$, $n = 1, \ldots, 16$. The results of numerical solution and analytical solution agree very well.

3.3. Schemes to implement pressure gradient

All the above accurate results were achieved through adding force term into the post-collision step. Here, we would also like to make further investigation on the two schemes to implement pulsatile pressure gradient. In Table I, the performance of two schemes was compared. Here, in all of the cases, $\alpha = 3.963$, mesh size $N_x \times N_r = 41 \times 41$, $T = 4800$ and the convergence criterion is Equation (16).

For the scheme of specifying inlet/outlet pressure, from the derivation in Appendix A, we notice that the value $L_x/(c_s T)$ should be very small so as to neglect the compressibility effect due to the time variation of pressure field [6]. In these cases, $T = 4800 \gg L_x/c_s = 40\sqrt{3}$, which satisfy the limit. The physical meaning is that in the range of the distance L_x, the time, T, during which the flow field undergoes a macroscopic change must be greater than the time, L_x/c_s [6].

From Table I, we can see that for the scheme of specifying pressure on inlet/outlet boundary, the overall average error increase with Δp between two ends or Reynolds number, which is consistent with the conclusion in paper [6]. For the scheme of adding forcing term, the overall average error decrease slightly with Δp. They also agree with Artoli *et al.*'s [5] results. It seems that the scheme of applying additional forcing term has more advantages than the scheme of specific pressure on inlet/outlet boundary for the 3D Womersley flow, which has uniform pressure gradient at any time.

3.4. Compressibility effect and comparison with Halliday's model

Here, the compressibility effect was investigated in detail. The quantity that represents compressibility is the mean variation of density. It is defined as

$$\Delta = \frac{1}{\rho_0} \sqrt{\sum_{x,t}((\rho(x,t) - \rho_0)^2)/N}$$

where the mean density is ρ_0 and N is the total number of nodes. For cases of $Re = 1200$, $\alpha = 7.927$, the mean density fluctuation Δ was calculated for $M_{max} = 0.218$, 0.109, 0.055 and 0.022. The M_{max} is the maximum Mach number in tube axis. In all simulations, $N_x \times N_r = 81 \times 81$, the Re and α were kept through varying T, p^* and τ value. The scheme of specifying inlet/outlet pressure was chosen to implement pressure gradient. The results of density fluctuation were listed in Table II. The table shows that for both models of Halliday and present,

$$\Delta(M_{max} = 0.055) \approx \tfrac{1}{4}\Delta(M_{max} = 0.109)$$

and

$$\Delta(M_{max} = 0.022) \approx \tfrac{1}{25}\Delta(M_{max} = 0.109)$$

These results agree with the known relationship [16] that Δ is proportional to M^2. Here we also find that when $M_{max} > 0.10$, the Δ of Halliday's model is slightly larger than that of present model.

It is also interesting to find some clues of compressibility effect through investigating the velocity field error. Here to investigate the velocity field error, four cases with $\alpha = 3.963$, $N_x \times N_r = 41 \times 41$, $T = 4800$ were simulated using both the present model and Halliday's model. The scheme of specifying inlet/outlet pressure was chosen to implement pressure gradient. Table III shows the velocity field error measured by θ and $\langle\theta\rangle$. θ at time t is defined as

$$\theta = \frac{\sum_i (u(r_i,t) - u_a(r_i,t))^2}{\sum_i u_a^2(r_i,t)} \tag{17}$$

Table II. Mean density fluctuation.

	Models	
Cases	Halliday's model Δ (%)	Present model Δ (%)
$M_{max} = 0.218,\ \tau = 0.9,\ p^* = 0.002,\ T = 1200$	6.807	6.651
$M_{max} = 0.109,\ \tau = 0.7,\ p^* = 0.0005,\ T = 2400$	1.658	1.642
$M_{max} = 0.055,\ \tau = 0.6,\ p^* = 0.000125,\ T = 4800$	0.412	0.412
$M_{max} = 0.022,\ \tau = 0.54,\ p^* = 0.00002,\ T = 12000$	0.0656	0.0656

Table III. The error of velocity field in 3D Womersley flow.

		Models			
		Halliday's model		Present model	
Cases		θ_{max}	$\langle\theta\rangle$ (%)	θ_{max}	$\langle\theta\rangle$ (%)
1	$Re = 120,\ p^* = 0.0001$	0.00534	0.054	0.00516	0.050
2	$Re = 240,\ p^* = 0.0002$	0.0131	0.172	0.0130	0.153
3	$Re = 600,\ p^* = 0.0005$	0.0942	0.923	0.0596	0.763
4	$Re = 1200,\ p^* = 0.001$	0.453	3.39	0.213	2.56

where the summation is over the diameter in middle pipe and the overall average error $\langle\theta\rangle$ is averaged over the period T. The θ_{max} means the maximum value of θ in a sampling period. In Table III, the M_{max} in tube axis for cases 1–4 are 0.054, 0.108, 0.272 and 0.544, respectively.

Comparing the maximum particular velocity error and the overall numerical average errors of two models in Table III, we observed that as M_{max} in tube axis increases, the corresponding errors of Halliday increases much faster than the present incompressible model. The observation is consistent with conclusion got for the standard and incompressible D2Q9 models [6]. Hence, comparing with Halliday's model, the present model can eliminate the compressibility effect.

3.5. Comparison with 3D LBGK

To show the performance of the proposed model, some cases were also simulated by the 3D incompressible LBGK model. The 3D simulation is based on the D3Q19 lattice velocity model. The mesh size used for the axisymmetric model is $N_x \times N_r = 81 \times 41$, while in the 3D LBM simulation, the mesh size used is $N_x \times N_y \times N_z = 81 \times 41 \times 41$. Notice in 3D simulations the curvature wall boundary treatment [14] was applied. In this comparison, we used two cases with parameters of $\alpha = 7.927,\ T = 1200,\ \tau = 0.6$ as examples. Table IV listed the overall numerical average error, period number to reach convergence criterion (16) and the CPU time required by the present axisymmetric model and 3D LBM.

All the computations were carried out on a supercomputer (Compaq ES40: total performance of 5300 Mflops) in the National University of Singapore. It can be observed from Table IV that the periodic number of iteration required by 3D LBM is slightly less than or equal to that of the axisymmetric model. However, the 3D LBM simulation takes about 110 times more computing time to obtain solutions than the present axisymmetric model. Hence, our proposed

Table IV. Comparison of CPU time and error between two LBGK model for 3D Womersley flow.

Cases	Models	To satisfy convergence criterion, total iterate period (T)	CPU (min)	$\langle \xi \rangle$
$Re = 1200$	3D (D3Q19)	24	338	1.288e-002
	2D (present model)	27	3.0	1.165e-002
$Re = 120$	3D (D3Q19)	24	281	1.193e-2
	2D (present model)	24	2.7	1.170e-2

model is much more efficient for such an axisymmetric pulsatile flow problem. According to the overall average error, the axisymmetric LBM result is slightly better than the 3D LBM result. One possible reason is that the axisymmetric model did not involve the error in the circumferential direction.

4. CONCLUSION

An axisymmetric incompressible LBGK model was derived in this paper by introducing an additional source term to the incompressible LBGK model [6]. With limit of Mach number $M \ll 1$ and $L_x/(c_s T) \ll 1$, this axisymmetric LBGK model successfully recovered the Navier–Stokes equation in the cylindrical coordinates through Chapman Enskog expansion (refer to Appendix A). For the additional source term in our model, most velocity gradient terms can be obtained from high-order momentum of distribution function, which is consistent with the philosophy of the LBM. The axisymmetric incompressible LBGK model was successfully applied to simulate the 3D pulsatile flow in circular tube and the spatial accuracy of the numerical solutions is about second order. Through the simulations with $1 < Re < 2000$ (Reynolds number is based on pipe's diameter), Womersley number $1 < \alpha < 25$, the axisymmetric incompressible LBGK model gives out very accurate results for 3D Womersley flow. Our model is valid for unsteady axisymmetric flows.

In our investigation, current LBGK model incorporating the extrapolation boundary condition and the forcing term is second order in space. Through comparison of the two schemes to implement pulsatile pressure gradient, it seems that the scheme of applying additional forcing term has advantages than the scheme of specify pressure on inlet/outlet boundary for the 3D Womersley flow, which has uniform pressure gradient at any time.

Through comparison with Halliday's axisymmetric model, it is observed that the present model can reduce the compressibility effect in Halliday's model because present model derived from the incompressible model [6]. Comparing with 3D LBGK model, present axisymmetric LBGK model gives out slightly better results than the 3D LBM and it is much more efficient than the 3D LBM in terms of computational time and memory.

APPENDIX A: CHAPMAN–ENSKOG DERIVATION OF THE AXISYMMETRIC INCOMPRESSIBLE D2Q9 MODEL

Here we show that the following continuity and Navier–Stokes equations may be obtained from a lattice Boltzmann D2Q9 model:

$$\frac{\partial u_x}{\partial x} + \frac{\partial u_r}{\partial r} = -\frac{u_r}{r} \tag{A1}$$

$$\frac{\partial u_\alpha}{\partial t} + u_\beta \frac{\partial u_\alpha}{\partial x_\beta} + \frac{1}{\rho_0} \frac{\partial p}{\partial x_\alpha} - v\nabla^2 u_\alpha = \frac{v}{r}\left(\frac{\partial u_\alpha}{\partial r} - \frac{u_r}{r}\delta_{\alpha r}\right) \tag{A2}$$

where α and β represent index x or r and x_α means x or r.

In the following equations, $f_i(x,r,t)$ is the distribution functions of D2Q9 model, the source term $h_i(x,r,t)$ was incorporated into an adjusted evaluation equation for the lattice fluid's momentum distribution (A3):

$$f_i(x + e_{ix}\delta_t, r + e_{ir}\delta_t, t + \delta_t) - f_i(x,r,t) = \frac{1}{\tau}[f_i^{(0)}(x,r,t) - f_i(x,r,t)] + h_i(x,r,t) \tag{A3}$$

Apply the Taylor expansion (A4) and expanding the time and space derivatives in terms of the Knudson number ε [17] in the following (A5):

$$f_i(x + e_{ix}\delta_t, r + e_{ir}\delta_t, t + \delta_t) = \sum_{n=0}^{\infty} \frac{\varepsilon^n}{n!} D^n f_i(x,r,t) \tag{A4}$$

$$
\begin{aligned}
f_i &= f_i^{(0)} + \varepsilon f_i^{(1)} + \varepsilon^2 f_i^{(2)} + \cdots \\
\partial_t &= \varepsilon\partial_{1t} + \varepsilon^2\partial_{2t} + \cdots \\
\partial_\beta &= \varepsilon\partial_{1\beta} \\
h_i &= \varepsilon h_i^{(1)} + \varepsilon^2 h_i^{(2)} + \cdots
\end{aligned}
\tag{A5}
$$

In (A5), there is no 'equilibrium' h_i term, where $\varepsilon = \delta_t$ and β can represent x or r and $D \equiv (\partial_t + \mathbf{e}_\beta \cdot \partial_\beta)$, we also notice that $\mathbf{e}_\beta \cdot \partial_\beta = \mathbf{e}_\beta \cdot \partial_{1\beta} = e_{ix}\partial_{1x} + e_{ir}\partial_{1r}$.

Incorporate (A4) and (A5) into (A3), in the zeroth, first and second orders of ε are (A6), (A7) and (A8), respectively:

$$E_i^0 = (f_i^0 - f_i^{\text{eq}})/\tau\delta_t \tag{A6}$$

$$E_i^1 = (\partial_{1t} + e_{i\beta}\partial_{1\beta})f_i^{(0)} + \frac{1}{\tau\delta_t}f_i^{(1)} - \frac{h_i^{(1)}}{\delta_t} \tag{A7}$$

$$E_i^2 = \partial_{2t}f_i^{(0)} + \left(1 - \frac{1}{2\tau}\right)(\partial_{1t} + e_{i\beta}\partial_{1\beta})[-\tau\delta_t(\partial_{1t} + e_{i\beta}\partial_{1\beta})f_i^{(0)} + \tau h_i^{(1)}]$$
$$+ \frac{1}{\tau\delta_t}f_i^{(2)} - \frac{h_i^{(2)}}{\delta_t} \tag{A8}$$

The equilibrium $f_i^{(0)}$ is defined by (6) and the distribution function f_i satisfied the following relationships:

$$\sum_{i=0}^{8} f_i^{(0)} = \frac{p}{c_s^2}, \quad \sum_{i=0}^{8} e_{i\alpha}f_i^{(0)} = \rho_0 u_\alpha \tag{A9}$$

$$\sum_{i=0}^{8} f_i^{(m)} = 0, \quad \sum_{i=0}^{8} \mathbf{e}_i f_i^{(m)} = 0 \quad \text{for } m > 0 \tag{A10}$$

A.1. Mass conservation and $h_i^{(1)}$

Summation of Equation (A7) over i leads to

$$\frac{1}{c_s^2}\frac{\partial}{\partial 1t}p + \rho_0\partial_\alpha u_\alpha = \sum_i \frac{h_i^{(1)}}{\delta_t} \tag{A11}$$

By rewriting (A11) in a dimensionless form, for the first term to be negligible, $L_x/(c_s T) \ll 1$ should be satisfied [6]. That is an additional limit of our derivation besides condition Mach number $M \ll 1$.

Summation of Equation (A8) over i leads to

$$\frac{1}{c_s^2}\frac{\partial}{\partial 2t}p = 0 \tag{A12}$$

and for simplicity, we assume

$$\sum_i \left(\tau - \frac{1}{2}\right)(\partial_{1t} + e_{i\alpha}\partial_{1\alpha})h_i^{(1)} - \sum_i \frac{h_i^{(2)}}{\delta_t} = 0 \tag{A13}$$

Compare (A11) with (A1) and notice $\sum_i \omega_i = 1$, following the selection of $h_i^{(1)}$ is reasonable.

$$h_i^{(1)} = -\frac{\omega_i \rho_0 u_r}{r}\delta_t \tag{A14}$$

Hence, at the same time, due to our assumption (A13), we obtain the following equation (A15):

$$\sum_i \frac{h_i^{(2)}}{\delta_t} = \left(\tau - \frac{1}{2}\right)\sum_i(\partial_{1t} + e_{i\alpha}\partial_{1\alpha})h_i^{(1)} = \delta_t\left(\tau - \frac{1}{2}\right)\left[\partial_{1t}\sum_i\left(-\frac{\omega_i\rho_0 u_r}{r}\right)\right]$$
$$= \delta_t\left(\frac{1}{2} - \tau\right)\left[\frac{1}{r}\partial_{1t}\rho_0 u_r\right] \tag{A15}$$

Notice that to derive (A15), we used equation $\sum \omega_i e_{i\alpha} = 0$.

A.2. Momentum conservation and $h_i^{(2)}$

Multiple Equation (A7) with $e_{i\alpha}$ and summation over i leads to

$$\rho_0\partial_{1t}u_\alpha + \partial_{1\beta}\Pi_{\alpha\beta}^0 = \sum_i \frac{h_i^{(1)}}{\delta_t}e_{i\alpha} = 0 \tag{A16}$$

where $\Pi_{\alpha\beta}^0 = \sum_{i=0}^{8} e_{i\alpha}e_{i\beta}f_i^{(0)} = \rho_0 u_\alpha u_\beta + c_s^2\rho\delta_{\alpha\beta}$.

So,

$$\rho_0\partial_{1t}u_r = -\partial_\beta\Pi_{r\beta}^0 = -\partial_\beta(c_s^2\rho\delta_{r\beta} + \rho_0 u_\beta u_r) \tag{A17}$$

Incorporate (A17) into (A15), we can get

$$(\text{VIP1}) \quad \sum \frac{h_i^{(2)}}{\delta_t} = \delta_t\left(\tau - \frac{1}{2}\right)\frac{1}{r}\partial_\beta(c_s^2\rho\delta_{r\beta} + \rho_0 u_\beta u_r) = \frac{3v}{r}\partial_\beta(c_s^2\rho\delta_{r\beta} + \rho_0 u_\beta u_r)$$

Multiply Equation (A8) with $e_{i\alpha}$ and summation over i lead to

$$\rho_0 \partial_{2t} u_\alpha + \left(1 - \frac{1}{2\tau}\right) \partial_{1\beta} \Pi_{\alpha\beta}^{(1)} = -\left(\tau - \frac{1}{2}\right) \left(\partial_{1t} \sum_i e_{i\alpha} h_i^{(1)} + \partial_{1\beta} \sum_i e_{i\alpha} e_{i\beta} h_i^{(1)}\right) + \sum_i \frac{h_i^{(2)}}{\delta_t} e_{i\alpha} \quad \text{(A18)}$$

To further derive Equation (A18), firstly we obtained (A19) and (A20):

$$\Pi_{\alpha\beta}^{(1)} = \sum_i e_{i\alpha} e_{i\beta} f_i^{(1)} = -\tau \delta_t \sum_i e_{i\alpha} e_{i\beta} D_{1t} f_i^{(0)} + \tau \sum_i e_{i\alpha} e_{i\beta} h_i^{(1)}$$

$$= -\tau \delta_t \left[\sum_i \frac{\partial}{\partial 1t} \Pi_{\alpha\beta}^{(0)} + \partial_k \left(\sum_i e_{i\alpha} e_{i\beta} e_{ik} f_i^{(0)}\right)\right] + \tau \sum_i e_{i\alpha} e_{i\beta} h_i^{(1)} \quad \text{(A19)}$$

$$\partial_k \left(\sum_i e_{i\alpha} e_{i\beta} e_{ik} f_i^{(0)}\right) = \rho_0 c_s^2 \partial_k (\delta_{jk}\delta_{\beta\alpha} + \delta_{j\alpha}\delta_{\beta k} + \delta_{j\beta}\delta_{\alpha k}) u_j = \rho_0 c_s^2 \left(\delta_{\alpha\beta}\partial_j u_j + \frac{\partial u_\alpha}{\partial x_\beta} + \frac{\partial u_\beta}{\partial x_\alpha}\right) \quad \text{(A20)}$$

In Equation (A18), the term $(\partial/\partial 1t)\Pi_{\alpha\beta}^0$ is of order M^2, (M is the Mach number), because if we assume the velocity of order u_0, length L, $t_0 = L/u_0$, then $(\partial/\partial 1t)\Pi_{\alpha\beta}^0 \sim u_0^2/t_0$, while the term $c_s^2(\partial u_\alpha/\partial x_\beta + \partial u_\beta/\partial x_\alpha)$ is of order $c_s^2 u_0/L$, hence, compare with term in (A20),

$$\frac{\partial}{\partial 1t} \Pi_{\alpha\beta}^0 \Big/ \text{term(A20)} = O\left(\frac{u_0^2}{t_0} \Big/ \frac{c_s^2 u_0}{L}\right) = O\left(\frac{u_0}{c_s}\right)^2 = O(M^2)$$

regarding the term $(\partial/\partial 1t)\Pi_{\alpha\beta}^0$ is very small, this term can be omitted.

$$\left(1 - \frac{1}{2\tau}\right) \Pi_{\alpha\beta}^{(1)} \approx -\tau\delta_t \left(1 - \frac{1}{2\tau}\right) \left[\rho_0 c_s^2 \left(\delta_{\alpha\beta}\partial_j u_j + \frac{\partial u_\alpha}{\partial x_\beta} + \frac{\partial u_\beta}{\partial x_\alpha}\right)\right]$$

$$+ c_s^2 \tau \delta_t \left(1 - \frac{1}{2\tau}\right) \left(-\frac{\delta_{\alpha\beta}\rho_0 u_r}{r}\right)$$

$$= -v \left[\rho_0 \left(\frac{\partial u_\alpha}{\partial x_\beta} + \frac{\partial u_\beta}{\partial x_\alpha} + \delta_{\alpha\beta}\left(\frac{u_r}{r} + \partial_j u_j\right)\right)\right]$$

$$= -v \left[\rho_0 \left(\frac{\partial u_\alpha}{\partial x_\beta} + \frac{\partial u_\beta}{\partial x_\alpha}\right)\right] \quad \text{(A21)}$$

in the above formula we used $\tau \sum_i e_{i\alpha} e_{i\beta} h_i^{(1)} = \tau\delta_t \sum_i e_{i\alpha} e_{i\beta}[-\omega_i \rho_0 u_r/r] = c_s^2 \tau\delta_t(-\delta_{\alpha\beta}\rho_0 u_r/r)$. The RHS term in (A18) is

$$\text{RHS} = c_s^2 \delta_t \left(\tau - \frac{1}{2}\right) \partial_{1\beta} \left(\frac{\delta_{\alpha\beta}\rho_0 u_r}{r}\right) + \sum_i \frac{h_i^{(2)}}{\delta_t} e_{i\alpha} \quad \text{(A22)}$$

Hence incorporate (A16), (A18), (A21) and (A22), we can obtain that

$$\rho_0 \frac{\partial u_\alpha}{\partial t} + \rho_0 u_\beta \frac{\partial u_\alpha}{\partial x_\beta} + \frac{\partial p}{\partial x_\alpha} - \rho_0 v \partial_\beta \left(\frac{\partial u_\alpha}{\partial x_\beta} + \frac{\partial u_\beta}{\partial x_\alpha}\right) = v \partial_{1\beta} \left(\frac{\delta_{\alpha\beta}\rho_0 u_r}{r}\right) + \sum_i \frac{h_i^{(2)}}{\delta_t} e_{i\alpha} \quad \text{(A23)}$$

Compare momentum equation (A23) with Equation (A2), to recover the Navier–Stokes momentum equation (VIP2) should be established:

$$\text{(VIP2)} \quad v \partial_{1\alpha} \left(\frac{\rho_0 u_r}{r}\right) + \sum_i \frac{h_i^2}{\delta_t} e_{i\alpha} = \frac{v}{r} \left(\partial_r \rho_0 u_\alpha - \frac{1}{r} \rho_0 u_r \delta_{r\alpha}\right)$$

Solving equation system (VIP1) and (VIP2), we can obtain the expression of $h_i^{(2)}$ as follows:

$$h_i^{(2)} = \delta_t \omega_i \frac{3v}{r} [\partial_\beta (c_s^2 \rho \delta_{r\beta} + \rho_0 u_\beta u_r)] + \delta_t \omega_i \frac{3v}{r} (\partial_r \rho_0 u_\beta - \partial_\beta \rho_0 u_r) e_{i\beta}$$

$$= \omega_i \delta_t \frac{3v}{r} \left[\partial_r \left(\frac{1}{3} \rho \right) + \rho_0 \partial_x u_x u_r + \rho_0 \partial_r u_r u_r + \rho_0 (\partial_r u_x - \partial_x u_r) e_{ix} \right] \quad (A24)$$

In the above derivation, we used Equation (A24):

$$\partial_\alpha \left(\frac{\rho_0 u_r}{r} \right) = \delta_{\alpha r} \partial_r \left(\frac{\rho_0 u_r}{r} \right) = -\delta_{\alpha r} \left(\frac{\rho_0 u_r}{r^2} \right) + \frac{\delta_{\alpha r}}{r} \partial_r \rho_0 u_r \quad (A25)$$

We successfully derived the expression of $h_i^{(1)}$ (A14), $h_i^{(2)}$ (A24) and recovered the continuity equation (A1) and Navier–Stokes equation (A2).

APPENDIX B: NOMENCLATURE

$c = \delta x / \delta t$	the ratio between lattice size and time step
$c_s = c/\sqrt{3}$	the speed of sound
$\mathbf{e}_i$	the particle velocity vector along direction i
f_i	the particle distribution function
h_i	the source terms
M	Mach number
N_r	number of lattice nodes in diameter
p	fluid pressure
p^*	the maximum amplitude of the oscillatory pressure gradient
Re	Reynolds number
R	the radius of the circular pipe
St	Strouhal number of Womersley flow
t	time
T	sampling period
U_{max}	the maximum velocity appear in tube axis during a sampling period
M_{max}	U_{max}/c_s
U_c	the characteristic velocity, which is equal to $(\alpha \to 0)$ or much larger than $(\alpha \gg 1)$ U_{max}
$\mathbf{u}$	fluid velocity vector
u_x	x component of the velocity
u_r	r component of the velocity
u_α	α component of the velocity, α can represent x or r

Greek letters

δx	lattice size
δt	time step
τ	the dimensionless relaxation time constant
ρ_0	fluid density
v	the kinetic viscosity of fluid
α	Womersley number
ω	angular frequency of Womersley
ω_i	weight coefficients for the equilibrium distribution function
ξ	velocity error defined by Equation (15)
$\langle \xi \rangle$	overall ξ averaged over a sampling period
θ	velocity error defined by Equation (17)
$\langle \theta \rangle$	overall θ averaged over a sampling period
σ	shear stress
Δ	the mean density fluctuation

REFERENCES

1. Chen S, Martinez D, Mei R. On boundary conditions in lattice Boltzmann methods. *Physics of Fluids* 1996; **8**:2527–2536.
2. Chen S, Doolen G. Lattice Boltzmann method for fluid flows. *Annual Review of Fluid Mechanics* 1998; **30**:329–364.
3. Halliday I, Hammond LA, Care CM, Good K, Stevens A. Lattice Boltzmann equation hydrodynamics. *Physical Review E* 2001; **64**:011208.
4. Hou S, Zou Q *et al*. Simulation of cavity flow by the lattice Boltzmann method. *Journal of Computational Physics* 1995; **118**:329–347.
5. Artoli AM, Hoekstra AG, Sloot PMA. 3D pulsatile flow with the lattice Boltzmann BGK method. *International Journal of Modern Physics C* 2002; **13**(8):1119–1134.
6. He X, Luo L. Lattice Boltzmann model for the incompressible Navier–Stokes equation. *Journal of Statistical Physics* 1997; **88**:3–4.
7. Guo Z, Shi B, Wang N. Lattice Boltzmann model for incompressible Navier–Stokes equation. *Journal of Computational Physics* 2000; **165**:288–306.
8. Cosgrove JA, Buick JM, Tonge SJ *et al*. Application of the lattice Boltzmann method to transition of oscillatory channel flow. *Journal of Physics A*: *Mathematical and General* 2003; **36**:2609–2620.
9. Artoli AM, Hoekstra AG, Sloot PMA. Accuracy of 2D Pulsatile flow in the lattice Boltzmann BGK method. *Lecture Notes in Computer Science* 2002; **2329**:361–370.
10. Maier RS, Bernard RS, Grunau DW. Boundary conditions for the lattice Boltzmann method. *Physics of Fluids* 1996; **8**(7):1788–1801.
11. Niu X, Shu C, Chew YT. An axisymmetric lattice Boltzmann model for simulation of Taylor–Couette flows between two concentric cylinders. *International Journal of Modern Physics C* 2003; **14**(6):785–796.
12. Guo Z, Zheng C, Shi B. Non-equilibrium extrapolation method for velocity and pressure boundary conditions in the lattice Boltzmann method. *Chinese Physics* 2002; **11**(4):366–374.
13. Zou Q, He X. On pressure and velocity boundary conditions for the lattice Boltzmann BGK model. *Physics of Fluids* 1997; **9**:1591–1598.
14. Guo Z, Zheng C, Shi B. An extrapolation method for boundary conditions in lattice Boltzmann method. *Physics of Fluids* 2002; **14**:2007–2010.
15. Bouzidi M, Firdouss M, Lallemand P. Momentum transfer of a Boltzmann-lattice fluid with boundaries. *Physics of Fluids* 2001; **13**(11):3452–3459.
16. Martinez DO, Matthaeus WH, Chen S, Montgomery DC. Comparison of spectral method and lattice Boltzmann simulations of 2D hydrodynamics. *Physics of Fluids* 1994; **6**(3):1285–1298.
17. Buick JM. Lattice Boltzmann methods in interfacial wave modelling. *Ph.D. Thesis*, The University of Edinburgh, 1997.